SANDIA REPORT

SAND2009-6169
Unlimited Release
Printed September, 2009

Quantifying Uncertainty from Material Inhomogeneity

Corbett C Battaile, Luke N Brewer, John M Emery, Brad L Boyce

Prepared by
Sandia National Laboratories
Albuquerque, New Mexico 87185 and Livermore, California 94550

Sandia is a multiprogram laboratory operated by Sandia Corporation,
a Lockheed Martin Company, for the United States Department of Energy's
National Nuclear Security Administration under Contract DE-AC04-94-AL85000.

Approved for public release; further dissemination unlimited.

Sandia National Laboratories

Issued by Sandia National Laboratories, operated for the United States Department of Energy by Sandia Corporation.

NOTICE: This report was prepared as an account of work sponsored by an agency of the United States Government. Neither the United States Government, nor any agency thereof, nor any of their employees, nor any of their contractors, subcontractors, or their employees, make any warranty, express or implied, or assume any legal liability or responsibility for the accuracy, completeness, or usefulness of any information, apparatus, product, or process disclosed, or represent that its use would not infringe privately owned rights. Reference herein to any specific commercial product, process, or service by trade name, trademark, manufacturer, or otherwise, does not necessarily constitute or imply its endorsement, recommendation, or favoring by the United States Government, any agency thereof, or any of their contractors or subcontractors. The views and opinions expressed herein do not necessarily state or reflect those of the United States Government, any agency thereof, or any of their contractors.

Printed in the United States of America. This report has been reproduced directly from the best available copy.

Available to DOE and DOE contractors from
U.S. Department of Energy
Office of Scientific and Technical Information
P.O. Box 62
Oak Ridge, TN 37831

Telephone: (865) 576-8401
Facsimile: (865) 576-5728
E-Mail: reports@adonis.osti.gov
Online ordering: http://www.osti.gov/bridge

Available to the public from
U.S. Department of Commerce
National Technical Information Service
5285 Port Royal Rd
Springfield, VA 22161

Telephone: (800) 553-6847
Facsimile: (703) 605-6900
E-Mail: orders@ntis.fedworld.gov
Online ordering: http://www.ntis.gov/help/ordermethods.asp?loc=7-4-0#online

SAND2009-6169
Unlimited Release
Printed September, 2009

Quantifying Uncertainty from Material Inhomogeneity

Corbett C Battaile, Luke N Brewer, John M Emery, Brad L Boyce

Abstract

Most engineering materials are inherently inhomogeneous in their processing, internal structure, properties, and performance. Their properties are therefore statistical rather than deterministic. These inhomogeneities manifest across multiple length and time scales, leading to variabilities, i.e. statistical distributions, that are necessary to accurately describe each stage in the process-structure-properties hierarchy, and are ultimately the primary source of uncertainty in performance of the material and component. When localized events are responsible for component failure, or when component dimensions are on the order of microstructural features, this uncertainty is particularly important. For ultra-high reliability applications, the uncertainty is compounded by a lack of data describing the extremely rare events. Hands-on testing alone cannot supply sufficient data for this purpose.

To date, there is no robust or coherent method to quantify this uncertainty so that it can be used in a predictive manner at the component length scale. The research presented in this report begins to address this lack of capability through a systematic study of the effects of microstructure on the strain concentration at a hole. To achieve the strain concentration, small circular holes (approximately 100 μm in diameter) were machined into brass tensile specimens using a femto-second laser. The brass was annealed at 450 ℃, 600 ℃, and 800 ℃ to produce three hole-to-grain size ratios of approximately 7, 1, and 1/7. Electron backscatter diffraction experiments were used to guide the construction of digital microstructures for finite element simulations of uniaxial tension. Digital image correlation experiments were used to qualitatively validate the numerical simulations. The simulations were performed iteratively to generate statistics describing the distribution of plastic strain at the hole in varying microstructural environments. In both the experiments and simulations, the deformation behavior was found to depend strongly on the character of the nearby microstructure.

Acknowledgment

The authors wish to thank Joel P McDonald for providing valuable contributions to this work. The authors would also like to thank their moms.

Contents

Acronyms **8**

Introduction **9**

Experiments **11**

Materials Fabrication 11

Electron Backscatter Diffraction 14

Digital Image Correlation 17

Summary 20

Simulation Results **25**

Model Generation and Theoretical Concerns 25

Crystal Plasticity Results and Statistics 26

Comparison with Traditional Incremental Plasticity 27

Summary 29

Discussion **33**

Conclusions **35**

Future Work **37**

References **38**

List of Figures

1 Pole figures from recrystallized brass as a function of grain size. 12

2 Drawing and image of tensile bar geometry. 13

3 In situ straining stage used for EBSD and DIC experiments. 14

4 Orientation and misorientation maps for $R = 7$. 15

5 Orientation and misorientation maps at 1% applied strain. 16

6 Orientation and misorientation maps at 2% applied strain. 17

7 Forward scatter images from the $R = 1/7$ sample after 2% applied strain. . . . 18

8 An EBSD image of the gauge section of a brass tensile bar with a 60 μm hole. 19

9 Analysis region for DIC, with EBSD image of the microstructure near the hole. 20

10 Schmid-Factor maps from EBSD data superimposed on the DIC analysis region. 21

11 Maps of the tensile strain component in the DIC analysis region. 21

12 A progression of DIC maps of the tensile strain component as the applied strain in the gauge section increases from 2% to 15%. 22

13 Maps of all three components of surface strain. 23

14 Polycrystalline mesh with a slot near its center. 26

15 Distributions of local plastic strain in a slotted polycrystalline mesh. 27

16 Equivalent plastic strain contour plot on a single crystal with a hole. 28

17 Probability density functions of the maximum plastic strain in a slotted polycrystalline mesh deformed to 1% applied strain. 29

18 Equivalent plastic strain emanating from the left and right corner of the notch. 31

19 Local view of the equivalent plastic strain emanating from the left and right corner of the notch. 32

20 Schematic of the uncertainty in materials property as a function of the ratio in characteristic length scales between critical phenomenon and internal structure. 34

List of Tables

1 Annealing Conditions for Brass 11
2 Crystal Plasticity Constants for Brass 30
3 Moments of the Distribution of Maximum Local Plastic Strain 30

Acronyms

DIC: digital image correlation

EBSD: electron backscatter diffraction

EDM: electro-discharge machining

LIMIS: local intragrain misorientation

LVDT: linear variable differential transformer

MEMS: micro-electro-mechanical systems

SEM: scanning electron microscope

Introduction

The combination of accurate physical models with high-performance computing has led to a new paradigm for the design, development, certification, production, and surveillance of weapons systems. Most of these models cull materials property data from a variety of sources to construct predictive, deterministic simulations of a variety of phenomena spanning structural, thermal, fluid, and shock mechanics. The material properties are generally treated as averaged, scalar values - i.e. "the" yield strength of brass - but most engineering materials are processed in ways that produce variations in their internal structure. These variations can occur on the microstructure scale (i.e. local differences in internal structure), on the component scale (i.e. from one region to another on the same part), from part to part (i.e. due to batch and lot variations), and over time as the material ages. Furthermore, these inhomogeneities can affect both properties and performance, producing uncertainty therein. Thus, it is often necessary to treat the process-structure-properties-performance spectrum *statistically*, and although this approach is often neglected, it can be critical to a predictive capability for assessing performance and reliability.

When a component's dimensions are comparable to the microstructural features in the constituent materials, e.g. in some micro-electro-mechanical systems (MEMS), the variability of material properties can drastically affect basic design quantities. For applications with dimensions spanning only a few grains, the local orientation of the crystalline microstructure can dominant properties. Furthermore, localized events, such as ductile crack nucleation and growth, can be particularly susceptible to the randomness of a material's microstructure. In ductile failure, crack incubation, nucleation, and growth typically occur by void formation and coalescence. Here again, the microstructure local to the material defect will dictate the peak load to crack initiation.

For ultra-high-reliability applications, the uncertainty in properties is compounded by a lack of data describing the extremely rare events that are often critical to the design criteria. Physical testing alone is often unable to supply sufficient data. For example, if reliability requirements demand no more than one in one-hundred failures, then "proof" from physical testing would require at least a hundred tests (and likely many more). Obviously, with realistic reliability requirements, performing a very large number of physical tests is usually prohibitive. Ideally, physical testing would be supplemented with a very large number of accurate, digital realizations that can be simulated (relatively) quickly and efficiently.

To date, there is no robust, coherent method to quantify this uncertainty and use it in a predictive manner at the component length scale. The present work aims to begin a systematic quantification of the effects of microstructure on uncertainty in plasticity and damage at engineered defects in brass. Brass was chosen for this study due to its relatively high elastic anisotropy [1], its availability, and the large catalogue of data describing its processing and properties. The approach couples tightly controlled experiments with high-throughput computing. First, experiments were used to directly observe the deformation behavior of microstructural features around through-holes in brass plates of varying grain sizes. Second, finite element simulations were used to probe the mechanisms underlying these observations, and to accumulate statistics describing the variability of strain concentration at defects in different microstructural environments. Third, as a first-order attempt to validate the simulation data, digital image correlation was used to compare the observed strain fields to the predicted ones.

Experiments

The results presented in this section are intended in part to answer the question, "Will the continuum prediction of the distribution of plastic deformation around a hole in tension, be valid regardless of the grain size of the underlying metal?" In a homogeneous continuum, the stress concentration associated with a cylindrical transverse through-hole in a finite plate is well known [2]. However, what happens when the hole is of a size comparable to or smaller than the microstructure? Does the hole dominate the strain field or do the local microstructural inhomogeneities dominate the strain field? To answer this question, in situ electron backscatter diffraction (EBSD) and digital image correlation (DIC) experiments were performed on brass plates with different grain sizes.

Materials Fabrication

The brass tensile bars for these experiments were produced from cold rolled, "cartridge" brass (70% Cu, 30% Zn) sheet material. Coupons of the brass were annealed using the conditions in Table 1. The heat treatment produced various grains sizes, and the crystallographic textures of the samples strengthened with increasing grain size (although the texture of the 800 ℃ / 8 hr sample was difficult to assess because of the large size of the grains). The brass had a consistent rolling texture of {110} rolling plane with a <111> rolling direction, as shown in Figure 1.

Tensile bars were machined from the recrystallized plates using electro-discharge machining (EDM) to achieve the sample dimensions drawn in Figure 2. Through holes were generated with an amplified Ti:sapphire pulsed laser, which had a pulse duration of 100 fsec (i.e. 10^{-13} sec), a central wavelength of 800 nm, a maximum average power of 1 Watt, and a pulse repetition rate of 1 kHz. The holes were nominally 100 μm in diameter. The laser beam was focused onto the surface of the specimen with a 10 cm plano-convex lens, yielding a focused beam diameter of approximately 60 μm. In order to produce circular through

Table 1. Annealing Conditions for Brass

Temperature [℃]	Time [hr]	Grain Size	Yield Strength [MPa]
450	8	19.3	126.9
600	8	79.1	126.9
800	8	725.2	126.9

Note: Twins were neglected in the grain size measurements.

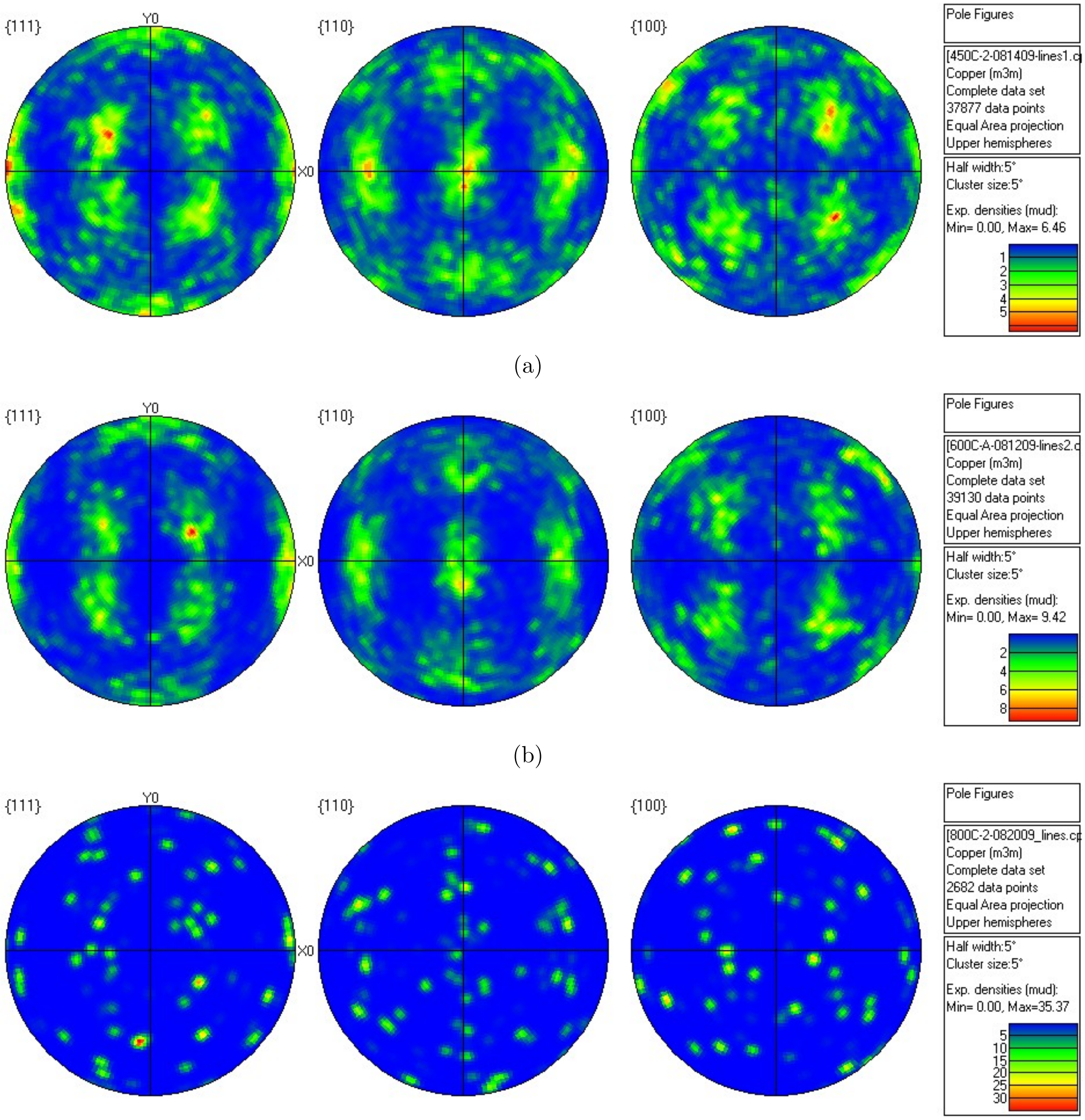

Figure 1. Pole figures from recrystallized brass as a function of grain size, for tensile bars annealed for 8 hr at a) 450 ℃, b) 600 ℃, and b) 800 ℃. X is both the rolling direction and the tensile direction.

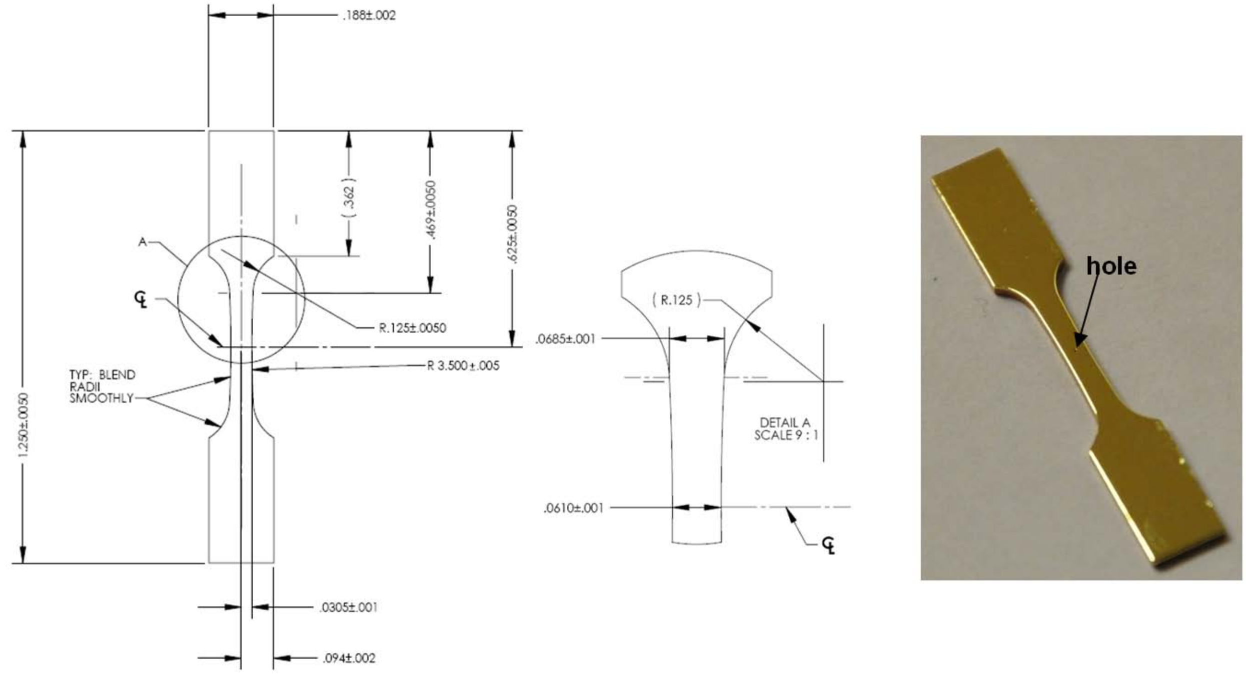

Figure 2. Drawing and image of tensile bar geometry. Dimensions are in inches. Note that the hole is present in the image but absent in the drawing.

holes, a circular iris aperture was placed before the focusing lens to select the center 5-6 mm of the 12 mm diameter beam emitted by the laser. Although the introduction of the circular aperture resulted in the production of a beam with diffraction fringes, the majority of the laser intensity remained in the central Airy disc. A laser pulse energy of 250-300 μJ (measured post-aperture) was used for drilling.

A variety of machining techniques were used (e.g. sample trepanning), but the optimum method for producing circular holes was simply percussive drilling in which the focused beam was moved 500 μm into the specimen along the direction parallel to the beam line [3]. The laser polarization was continuously rotated at a rate of 20 °/sec using a half-waveplate [4]. At the laser pulse energy of 250-300 μJ, the penetration rate was approximately 3.5 μm/sec. Because the aspect ratios of the through-holes were relatively large (i.e. approximately 10:1), the diameter of the hole at entry was generally larger than that at exit. Attempts to remedy this by repeating the machining process in the same location on the opposing face, proved unsuccessful due to difficulties with precision alignment.

After laser machining, the tensile bars were prepared for electron microscopy using starndard metallographic techniques. Both sides of the sample were coarsely ground to produce an approximately flat surface. One side of each sample was then further polished to a 1 μm diamond finish, and then finally electropolished.

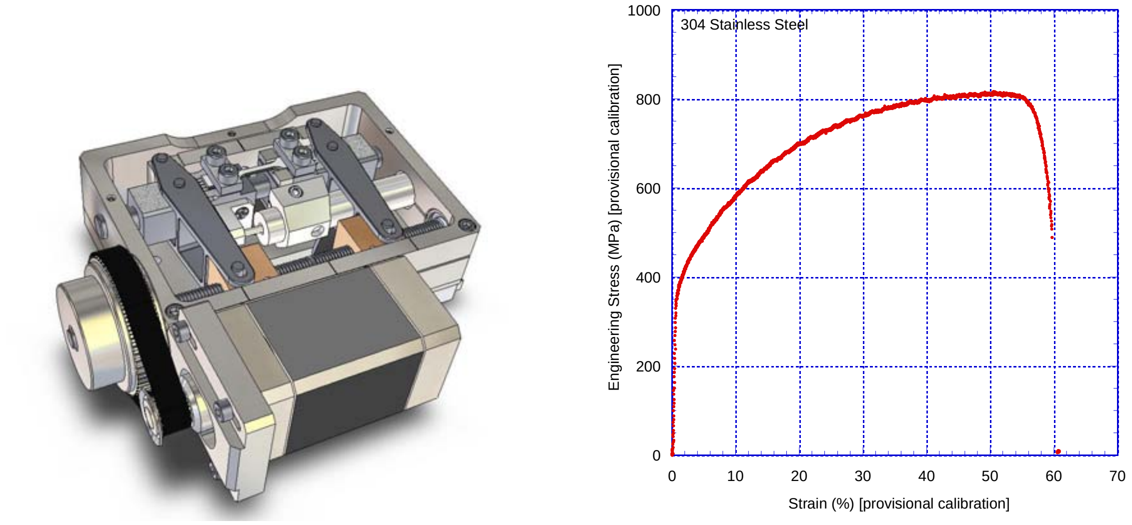

(a) (b)

Figure 3. a) In situ straining stage used for EBSD and DIC experiments. b) Example stress-strain curve from 304 stainless steel.

The *in situ* mechanical testing was performed in a Zeiss Supra 55 VP-FEG scanning electron microscope (SEM). The straining stage was specifically designed and built at Sandia National Laboratories, and has a unique design and footprint specifically engineered for SEM-EBSD experiments. The stage uses a linear variable differential transformer (LVDT) for measuring displacement, and a whetstone bridge transducer for measuring load. A drawing of the stage, and results from a test on a 304 stainless steel sample of the same dimensions as the brass bars used in the present study, are pictured in Figure 3. This stage was used for both the EBSD and DIC measurements.

Electron Backscatter Diffraction

Electron backscatter diffraction was used to construct maps of the crystallographic orientation around the hole after the samples were subjected to strain-controlled, uniaxial tension. The EBSD measurements were performed in the Zeiss Supra 55 VP SEM using the HKL Channel 5 EBSD system with a Nordlys-II camera. The maps were measured at a 20 keV beam energy with 8x8 binning of the pattern and a frame time in the range of 4-9 msec. The step size for each map varied depending on the grain size of the material. As seen in Table 1, the grain sizes of the three specimens varied by more than an order of magnitude. The hole size also varied, partly because of the holes' conical shapes (see above) and the grinding of the specimen. The holes ranged in diameter from 80-120 μm. In the following discussion, the hole size is normalized by the grain size using the ratio,

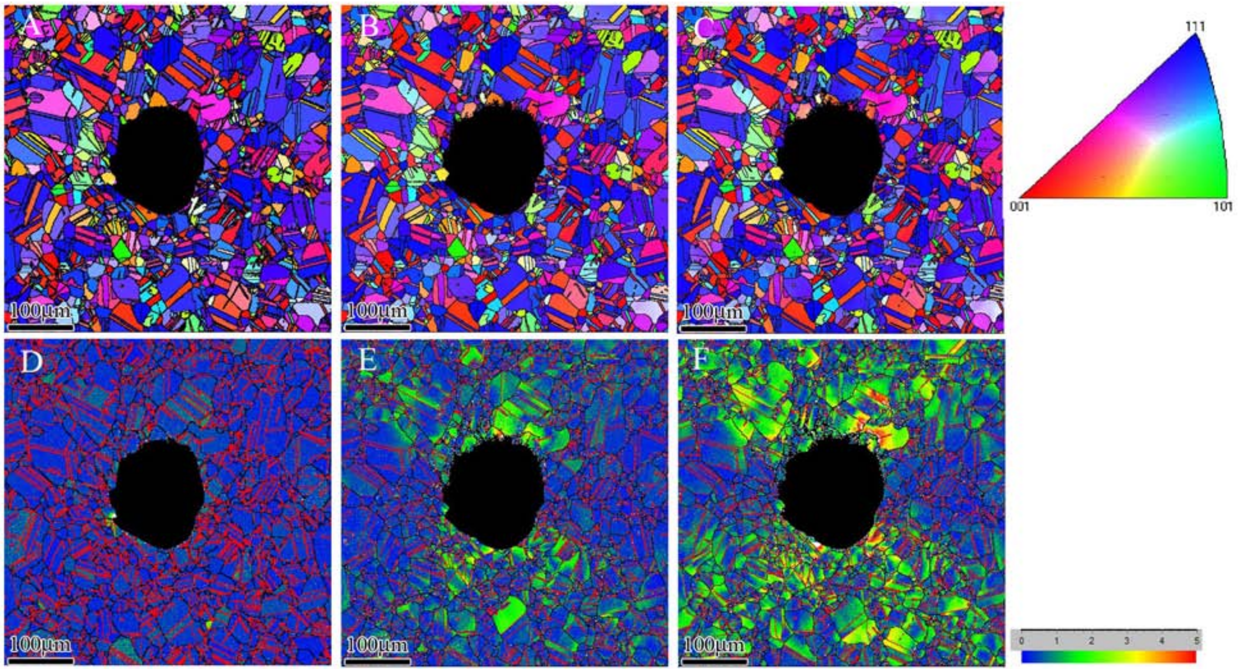

Figure 4. a-c) Orientation (inverse pole figure with respect to loading axis) and d-f) local intragrain misorientation (LIMIS) maps from the $R = 7$ sample. From left to right: no applied strain, 1% applied strain, and 2% applied strain.

$$R = \frac{\text{hole size}}{\text{grain size}}. \tag{1}$$

In the present work, this ratio is within $R \in (0.1, 10.0)$.

The orientation maps from the EBSD experiments clearly show the expected concentration of plastic deformation around the hole for a ratio of $R = 7$, i.e. for a hole surrounded by finer grains, as depicted in Figure 4. While EBSD cannot directly measure plastic strain, it can map and measure the crystallographic rotation produced by plastic strain. There are many ways to map plasticity-induced crystallographic rotation, but here we use the local intragrain misorientation map [5]. In this representation, deformation is plotted as an angular misorientation, with greater misorientation representing larger crystallographic rotation and therefore larger plastic deformation. In Figure 4, it is obvious that the zones of largest misorientation lie approximately perpendicular to the tensile axis, as expected. It is important to note, however, that even within the lobes of plastic deformation, the amount and distribution of misorientation varies substantially from grain to grain.

As the R ratio (Equ 1) decreases, we do not see the expected distribution of misorientation or plastic deformation around the holes, as shown in Figure 5 and 6. At 1% applied strain

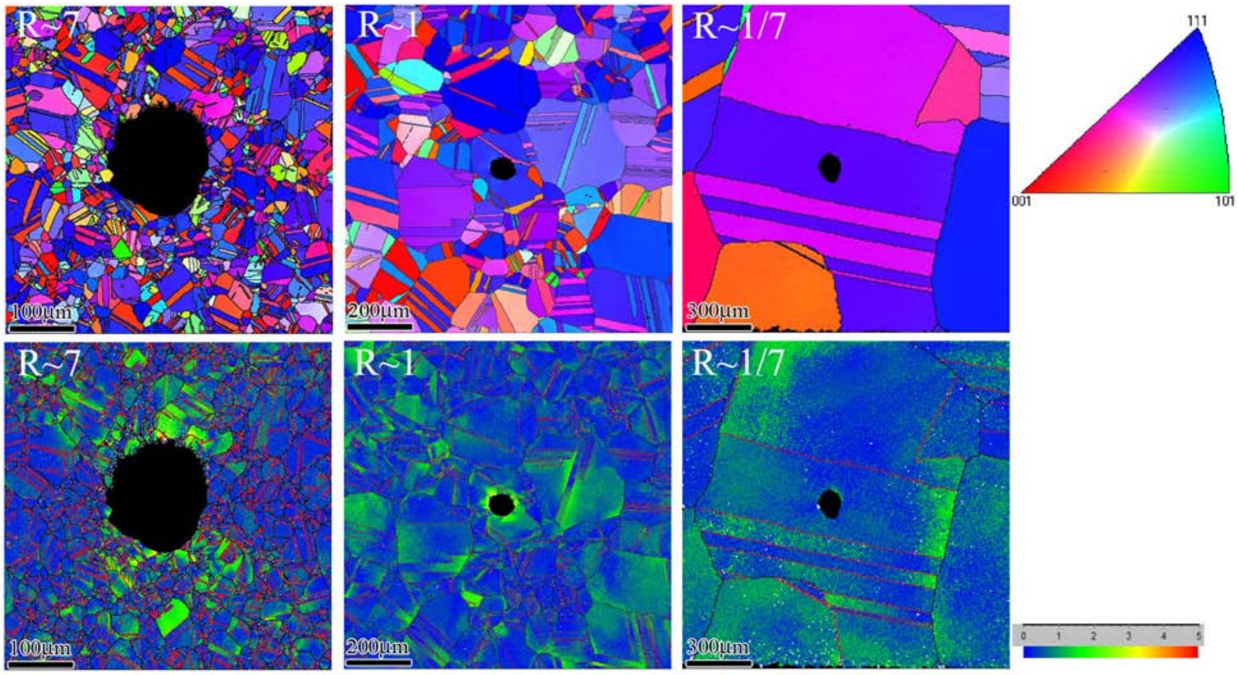

Figure 5. Orientation (i.e. inverse pole figure with respect to loading axis) and local intragrain misorientation (LIMIS) maps for three different R ratios. All maps correspond to tensile bars with 1% applied strain.

(Figure 5), there is only a slight strain concentration around the hole for $R = 1$, and no observed concentration for $R = 1/7$. It should be noted, however, that the yield strength of brass decreases considerably as the R ratio decreases in these experiments, since the corresponding grain size increases (see Equ 1 and Table 1). Therefore, more plasticity might be expected at the larger grain sizes. However, a lack of observed misorientation does not necessarily indicate a lack of plasticity. For example, conditions of pure shear, single slip, or double slip might not generate observable lattice rotation (see below).

As the applied strain is increased to 2%, more misorientation is observed (Figure 6). In the $R = 7$ sample, the lobes of misorientation grow in intensity and somewhat in size. Misorientation is observed throughout the microstructure for the $R = 1$ sample, and is pronounced in grains away from the hole, suggesting that the hole is not concentrating significant strain. In the $R = 1/7$ sample, lobes of misorientation do appear to be emanating from the hole, but do not appear to be interacting strongly with the local crystallography of the grain containing the hole. The lobes of misorientation at the hole do not lie in the orientation (relative to the tensile axis) expected from a consideration of continuum plasticity. However, the slip traces on the surface of the $R = 1/7$ sample do suggest that significant plasticity is taking place through single and double slip on specific slip planes, as shown in Figure 7.

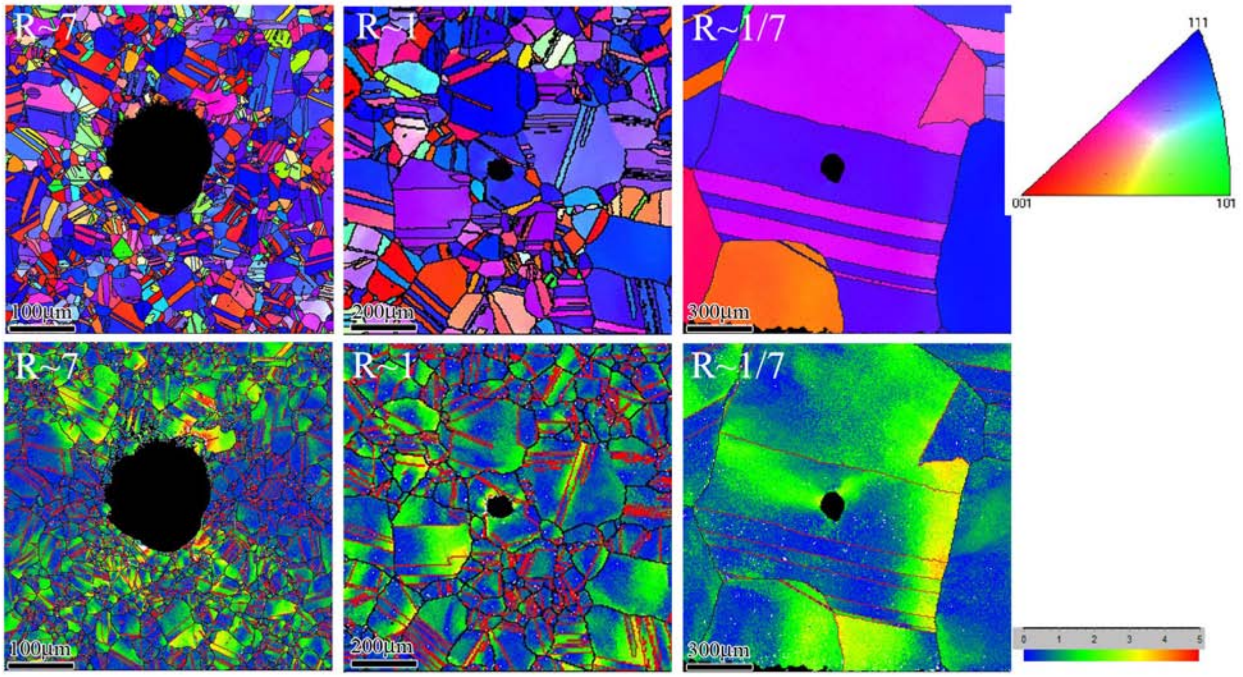

Figure 6. Orientation (i.e. inverse pole figure with respect to loading axis) and local intragrain misorientation (LIMIS) maps for three different R ratios. All maps correspond to tensile bars with 2% applied strain.

Digital Image Correlation

To characterize the actual local strain fields within individual grains and around a small hole, we employed a recently developed microscale digital image correlation (μDIC) technique. Microscale DIC is based on a standard optical-image-based DIC [6], which has been employed in our labs for numerous studies including the examination of deformation behavior in sub-millimeter weldments [7]. The two-dimensional variant of DIC compares images from a field of speckle contrast viewed from a single camera to determine the planar deformation field. A key to successful DIC at any scale lies in the ability to produce stable "speckles" that can move with the material deformation. At the microscale, ductile metals typically form slip steps during high-strain deformation, and this can confound DIC analysis. Therefore, we dispersed 1 μm gold particles on the surface of the brass tensile bar. Under EBSD conditions, there is strong contrast between the gold and brass materials (so-called "Z-contrast"), while the topographical contrast created by slip steps is much weaker. Figure 8 shows an EBSD image of gold powder particles dispersed on the surface of brass.

Rectangular, 350x450 μm fiduciary boxes were drawn on both sides of the laser-machined holes by dragging a tungsten needle on the brass surface using a 3-axis motorized micromanipulator tool. These boxes permitted precise registry between EBSD imaging of the crystal

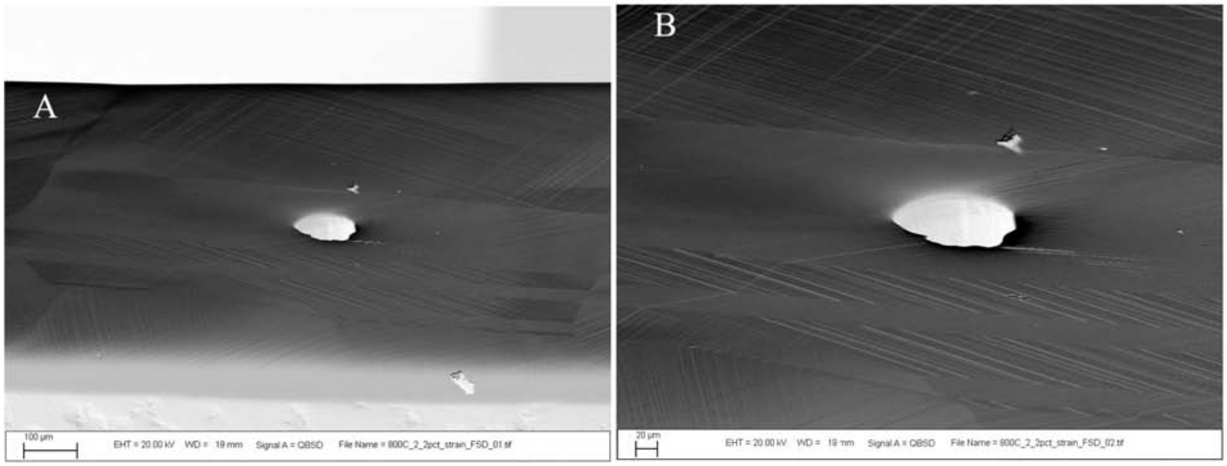
A
B
100 µm
EHT = 20.00 kV WD = 19 mm Signal A = QBSD File Name = 800C_2_2pct_strain_FSD_01.tif
20 µm
EHT = 20.00 kV WD = 19 mm Signal A = QBSD File Name = 800C_2_2pct_strain_FSD_02.tif

Figure 7. Forward scatter images from the $R = 1/7$ sample after 2% applied strain. The lines on the surface are slip traces due to plastic deformation.

structure and μDIC mapping of the surface deformation and strain fields. The outline of these boxes is subtlety visible in Figure 8, and was used to define the DIC analysis region, shown as a red box in Figure 9. The image axes in Figure 9 were carefully aligned with the tensile axes, revealing that the fiduciary boxes were actually tilted slightly from the tensile axes. This imperfection in alignment is inconsequential to the analysis, since the DIC analysis relies on the image axes to define the reference coordinate system, and is independent of the axes of the analysis window. The spatial relationship between the fiduciaries, the DIC analysis window, and the EBSD crystallographic data is shown in Figure 10, which contains a grayscale Schmid-factor map that clearly delineates the grain and twin structures in relation to the hole and the analysis window.

The DIC technique does not measure the strain at every pixel, but rather uses a collection of pixels (called a subset window) to determine local deformation and strain. In this analysis, the subset window was chosen to be 15x15 μm in size (41x41 pixels) so that each subset of the analysis region contained a sufficient number of contrasting speckles to permit DIC analysis. Hence, deformation gradients which occur over scales smaller than 15 μm, are inherently "smeared" by the analysis. For example, a sharp crack opening under a tensile load would typically appear as a high deformation region, rather than an actual discontinuity in deformation and strain. This smearing of the strain fields is somewhat unfortunate for this particular study, since it is a confounding factor when imaging the local strains within the smaller grains and the strain concentration in the immediate vicinity of the hole. Future efforts will focus on applying a finer speckle pattern, such as 100 nm gold powder particles, to permit higher spatial strain resolution. Nevertheless, the influence of the microstructure on deformation near the hole is clearly evident (see below).

Figure 11 contains a comparison of the the tensile strain component (σ_{yy}) in two different

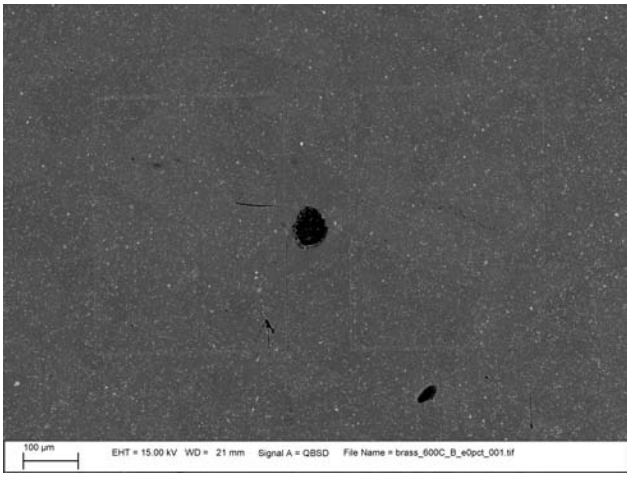
100 μm
EHT = 15.00 kV WD = 21 mm Signal A = QBSD File Name = brass_600C_B_e0pct_001.tif

Figure 8. An EBSD image of the gauge section of a brass tensile bar with a 60 μm hole. The white dots are gold particles. Note the rectangular boxes that are faintly visible on both the right and left sides of the hole. These boxes are used as fiduciaries to align DIC data with EBSD data.

brass microstructures (labeled 800 ℃and 600 ℃). Both strain-field images were taken after 9% applied strain.

The coarse-grained sample annealed at 800 ℃ (Figure 11(b)) shows a region of low tensile strain (blues and purples in the color spectrum) near the hole, with an edge that is clearly defined by the grain boundary (see Figure 10(b)). The grain surrounding the hole has a low Schmid factor, and is therefore poorly oriented for deformation (i.e. is a so-called "hard"" grain). The surrounding grains, by comparison, have higher Schmid factors and thus exhibited much higher strain values (greens and yellows). The strain-concentrating effect of the hole is also clearly visible: lobes on the right and left sides of the hole show regions of elevated tensile strain and lobes on the top and bottom of the hole show regions of suppressed tensile strain (i.e. superposed compression). Note that the magnitude of the strains at the hole are comparable to those in the surrounding microstructure.

The fine-grained sample annealed at 600 ℃ (Figure 11(a)) shows a similar behavior, in that the strains at the hole are comparable in magnitude to those in the surrounding microstructure. In this fine-grained sample, the smearing effect makes a direct connection between strain fields and grain Schmid factors more difficult.

The DIC maps in Figure 11 show only one component of local strain at a single value of the applied strain. The DIC data collected in this study include all three components of the surface strain tensor at applied strains from 1% to 15%. For example, Figure 12 shows a progression of the local tensile strain component (σ_{yy}) with a fixed color scale at applied strains from 2% to 15%. At 15% applied strain, some of the strain data is missing because

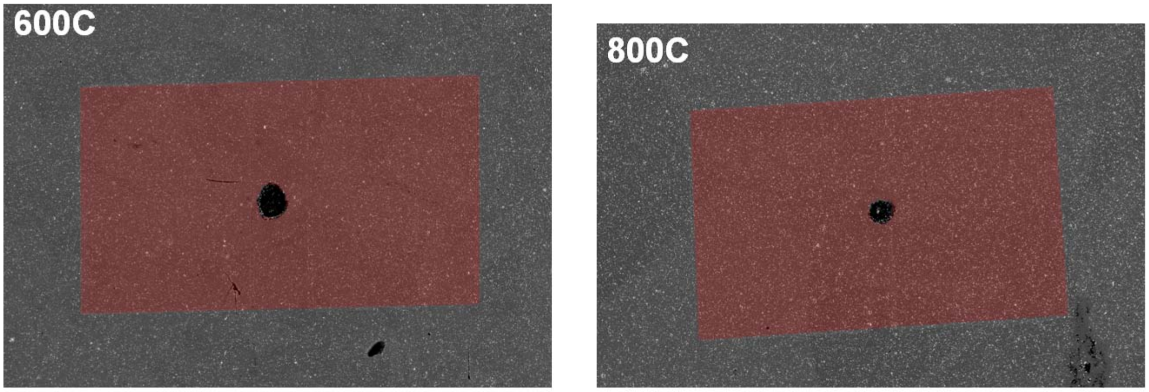

(a) (b)

Figure 9. Analysis window (red) for DIC, superimposed on EBSD image of the region surround the hole in tensile bars annealed at a) 600 ℃ and b) 800 ℃.

of slip-step contrast in the image (see above). Figure 13 shows all three components of strain (σ_{xx}, σ_{yy}, and σ_{xy}) at a single applied strain of 12%. Again, the same conclusions are supported in all three strain fields: the expected lobes formed near the hole (notice the 45° lobes in the shear strain data), but the superimposed microstructural strains are comparable to the local strains at the hole.

Summary

Both the EBSD and DIC measurements show the strong effect of microstructure and local crystallography on the strain concentration of a hole in a plate. Microstructures with fine grains with respect to the hole size (i.e. $R >> 1$), exhibited the lobes of plastic deformation expected from a consideration of continuum mechanics. However, as the R ratio became less than 1 (i.e. a small hole in large grains), the behavior became far more complicated. Digital image correlation indicated that the strain lobes predicted by continuum mechanics are still present, but they are comparable in magnitude to the strains in neighboring grains which are more favorably oriented for slip. These results present initial evidence that greater care will need to be taken in predicting the strain concentration effects of defects as they approach the characteristic size of the underlying microstructure.

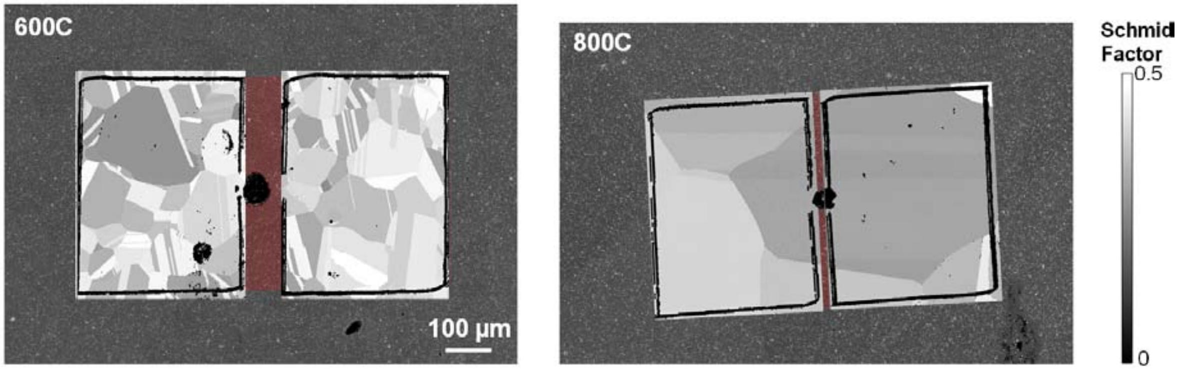

(a)

(b)

Figure 10. Schmid-Factor maps from EBSD data superimposed on the DIC analysis region, for tensile bars annealed at a) 600 ℃ and b) 800 ℃. Note that dark grey grains with the lowest Schmid factor are expected to be the hardest to deform (specifically, requiring the highest tensile stresses to activate the first slip system).

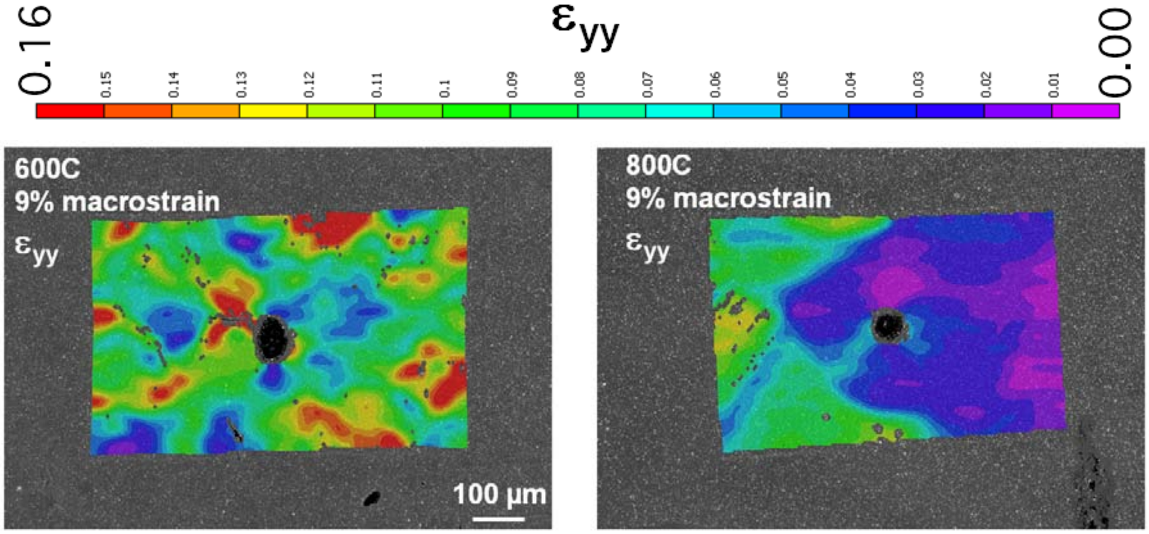

(a)

(b)

Figure 11. Maps of the tensile strain component (σ_{yy}) in the DIC analysis region, for tensile bars annealed at a) 600 ℃ and b) 800 ℃. Note that the low-strain region in (b) corresponds to the low Schmid-Factor grain in Figure 10(b). Both maps were taken when the strain in the gauge section was approximately 9% based on stroke data.

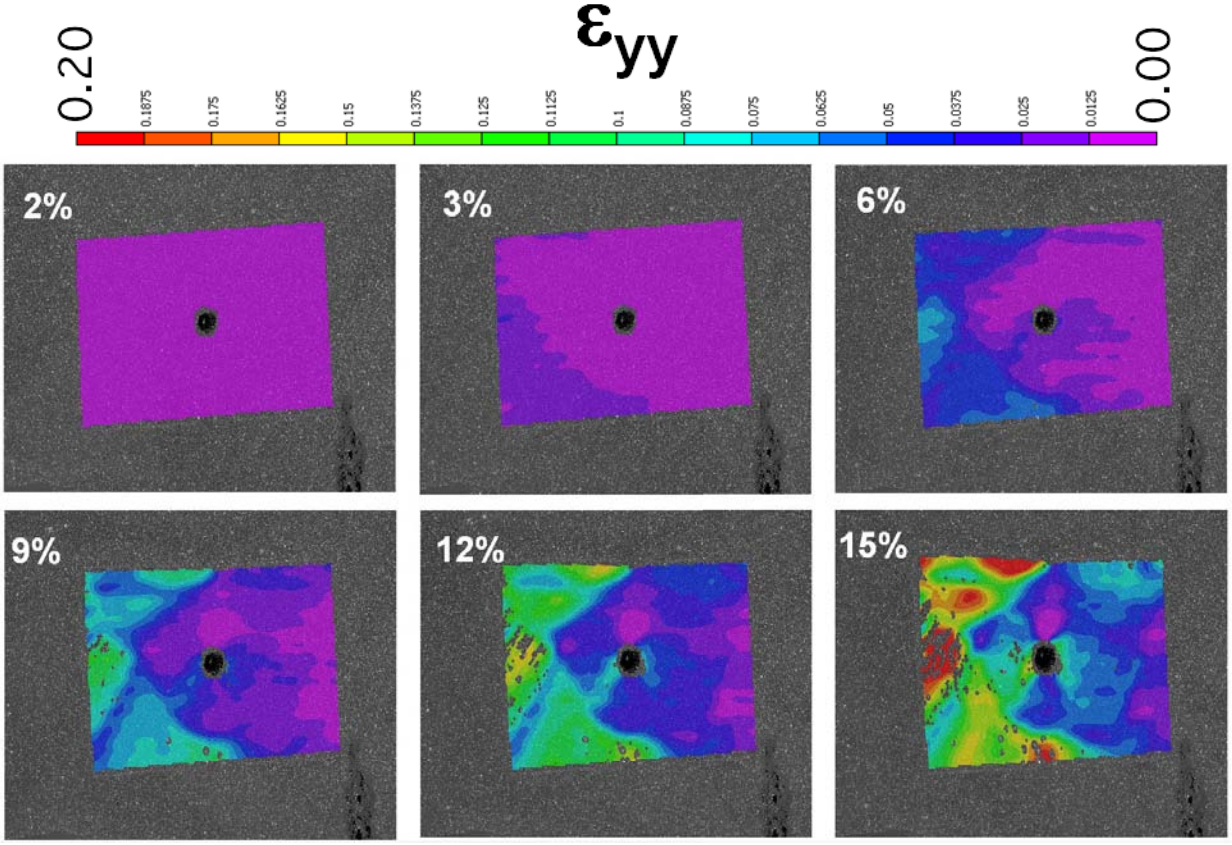

Figure 12. A progression of DIC maps of the tensile strain component (σ_{yy}) as the applied strain in the gauge section increases from 2% to 15%, for a tensile bar annealed at 800 ℃.

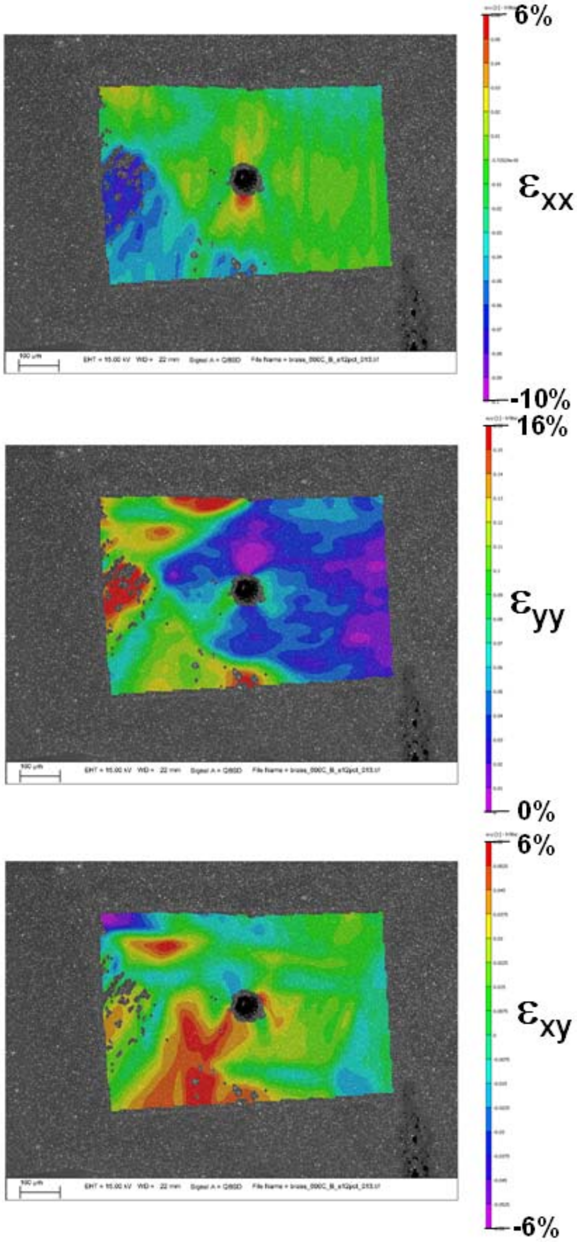

Figure 13. Maps of all three components of surface strain (σ_{xx}, σ_{yy}, and σ_{xy}), for a tensile bar annealed at 800 ℃ and deformed to 12%. applied strain.

Simulation Results

Crystal plasticity simulations were completed to explore the effects of random texture on strain concentrations. In these simulations, detailed finite element models of representative microstructures were used and the crystallographic orientations of individual grains were varied. Comparison of these simulations with the experimental results provides qualitative validation of the crystal plasticity model. Further, comparison of the crystal plasticity models to traditional J2-plasticity illustrates the impact of the random texture on the local strain field.

Model Generation and Theoretical Concerns

To ascertain the sensitivity of a defect's strain concentration to its crystallographic environment, a slot with rounded caps was placed in a finite element model of a pollycrystalline material, as depicted in Figure 14. The mesh contains 205,147 elements, with one element through the thickness (i.e. in the Z-direction). The length of the slot is approximately 38, the radius of curvature of its caps is approximately 3, and the average grain size of the polycrystal is 6.87 (computed as the square root of the average area), all in arbitrary units for the present purpose. Taking the equivalent hole size to be 6, and the grain size to be 6.87, produces an R ratio of approximately $R = 0.87$. The geometry in Figure 14 was created by performing a two-dimensional, Monte Carlo Potts simulation of ideal, normal grain growth [8] on a lattice of 256x256 sites, and then generating the mesh topology by fitting the (inherently pixellated) grain boundaries to natural cubic splines.

A polycrystal plasticity constitutive model [9], with material parameters fit to tensile test data for brass [10], was used in the calculations. Two hardening models [9] and two types of boundary conditions (see below) were employed, and the constitutive model parameters are listed in Table 2. The equation governing the evolution of the critical resolved shear stress (i.e. the hardness) in power law hardening is

$$\tau_{crss} = \tau_{crss,o} + A\epsilon_p^n, \tag{2}$$

and that in Voce hardening is

$$\tau_{crss} = \tau_{crss,o} + A[1 - exp(-n\epsilon_p/A)], \tag{3}$$

where ϵ_p is the equivalent plastic strain, and the other variables are defined in Ref [9] and enumerated in Table 2.

Crystal Plasticity Results and Statistics

Before examining the results from a complex polycrystal, it is instructive to examine simpler calculations for a cylindrical hole embedded within a single, square crystal. For these calculations, the orientation of the single crystal was varied to study its effect on the strain concentration. The displacements were fixed in the Z-direction on the positive and negative Z-face and 1% global strain was applied in the X-direction. There were 3663 elements in the mesh. Figure 16 shows the result for four crystallographic orientations. Figure 16(a) corresponds to a crystal whose principal axes are parallel to those of the global coordinate system. Bands of plastic deformation emanate at 45° from the hole. Figure 16(b) corresponds to a crystal whose principal axes are rotated 45° about the reference Z-axis. This orientation causes the plastic deformation to diffuse into the crystal. Figure 16(c) corresponds to a crystal whose orientation is chosen from a set of observed orientations, but remains closely aligned to the global axes. Clear bands of plastic deformation form, but the peak plastic strain is lower than in Figure 16(a). Finally, Figure 16(d) corresponds to a crystal whose orientation is not closely aligned with the global axes. Again, clear bands of plastic deformation are formed; however, these bands do not lie along the 45° lines.

The finite element model shown in Figure 14 was used to perform simulations of uniaxial tension to 1% applied strain in the Y-direction (i.e. perpendicular to the length of the slot). Many such simulations were performed, and in each, the crystallographic orientation

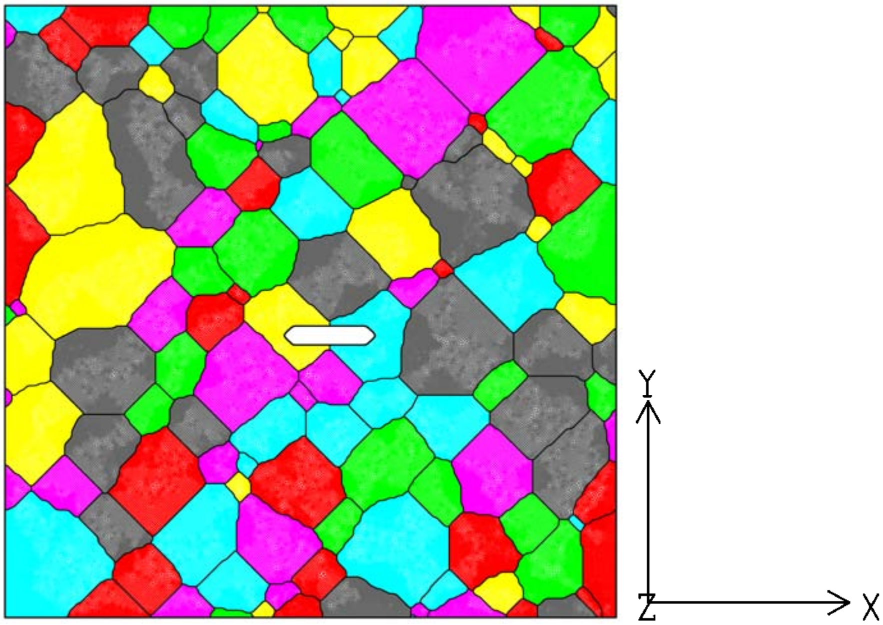

Figure 14. Polycrystalline mesh with a slot near its center. Different colors denote different grains with distinct crystallographic orientations.

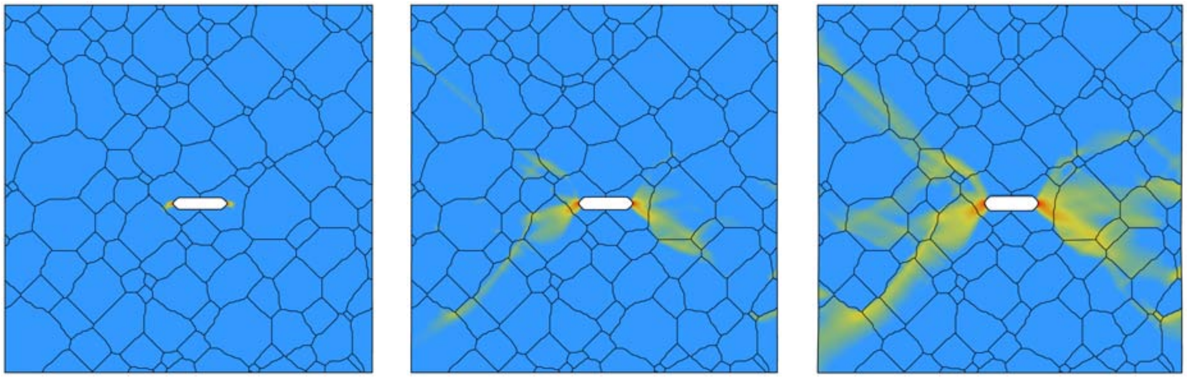

(a) (b) (c)

Figure 15. Distributions of local plastic strain in a slotted polycrystalline mesh deformed to a) 0.2%, b) 0.5%, and c) 1.0% applied strain. The tensile axis was perpendicular to the length of the slot.

of each grain was assigned from a uniform random distribution. An example is depicted in Figure 15, which shows the distribution of local plastic strain, and its perturbation by the microstructural environment, for three values of the applied strain.

The probability distributions of the maximum plastic strain per simulation, are shown in Figure 17. (The "bonded" boundary condition corresponds to the constraint of a single plane of nodes, perpendicular to the Z-direction, such that their Z-displacement was prohibited.) The first and second moments of the distributions are shown in Table 3. Note that for Voce hardening, the standard deviation of the distribution is nearly 20% of its mean. This observation is alarming in and of itself, since it means that a relatively moderate stress concentrator (e.g. compared to a crack) like a rounded slot with aspect ratio $6\frac{1}{3}$, can produce local plastic deformation that varies significantly depending on the microstructural environment.

Comparison with Traditional Incremental Plasticity

For purposes of comparison, the equivalent plastic strain concentration was computed in the notched specimen using von Mises yield criterion with a power law, isotropic hardening model. The parameters to describe the J2-plasticity were set to match the average response of a polycrystal with no notch, the unotched version of that shown in Figure 14. Figure 18 shows the equivalent plastic strain versus distance from the left and right corners of the notch. Here, five crystal plasticity results, representing various probabilities of occurrence, are plotted with the J2 results. Along the path, the effect of the grain boundaries is apparent by the roughness of the crystal plasticity results. Further, for 1% applied global strain, the

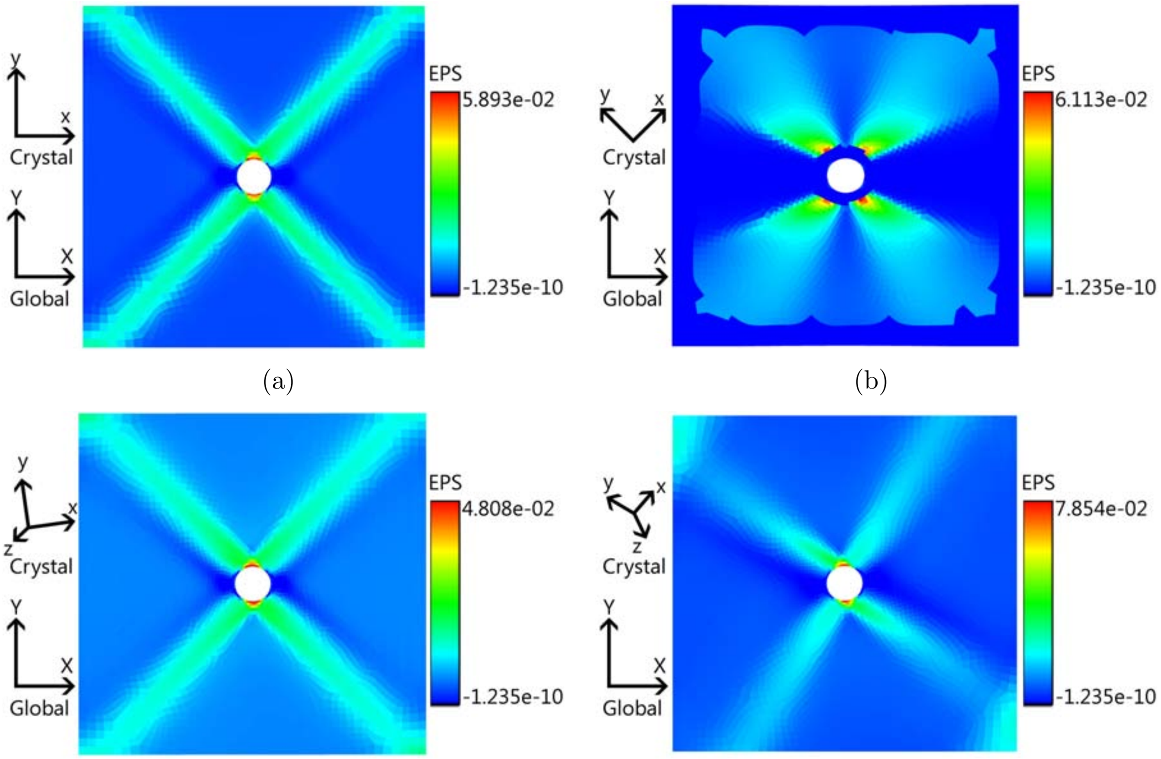

(a) (b) (c) (d)

Figure 16. Equivalent plastic strain contour plot on a single crystal with a hole. (a) Crystal aligned with the global axes. (b) Crystal rotated 45 degrees in the global XY-plane. (c) Random observed crystal orientation closely aligned with the global axes. (d) Random observed crystal orientation.

peak strain concentration appears to be contained within the first grain at the notch tip. However, the differences in strain concentrations near the notch is hidden due to the scaling of the plots.

Figure 19 shows a local view of the equivalent plastic strain versus distance. In addition, there is a dashed line which represents a least squares fit of the data. This fit is used to extrapolate the concentration to the edge of the notch. Here the differences in strain concentrations for the crystal plasticity results are apparent. Of particular interest are the results from crystal plasticity realizations #4 and #5. For realization #4, the peak strain clearly occurs at the left corner of the notch; however, for realization #5, the peak strain occurs at the right corner. Due to a slight eccentricity caused by the location of the notch, the strain concentration predicted by J2 is not identical for the left and right corners; however, it is very similar. The J2 strain concentration is consistently lower than the crystal plasticity results. This may indicate that a better fit for the J2 material parameters is required (*e.g.* larger RVE or lower tolerances) and leaves room for future work. However, prior experience

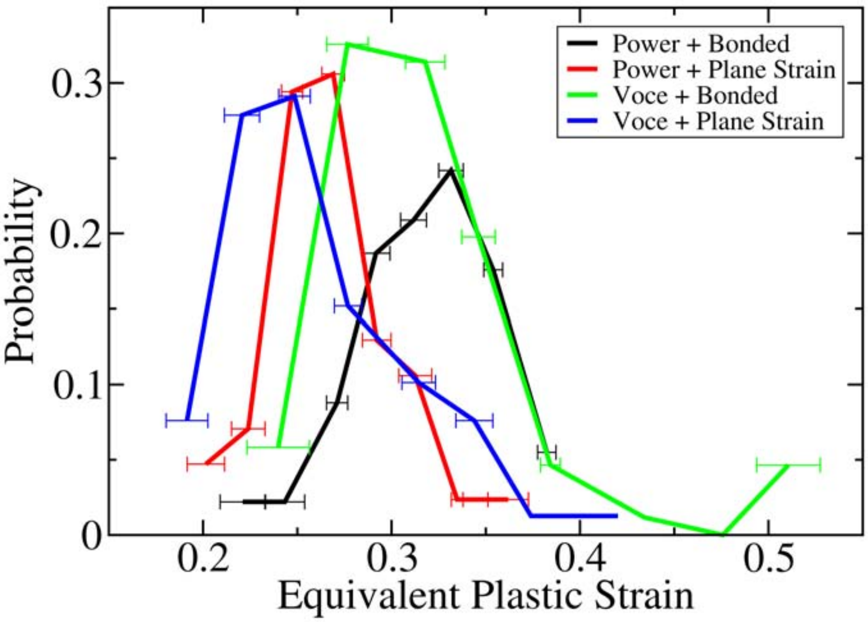

Figure 17. Probability density functions of the maximum plastic strain in a slotted polycrystalline mesh deformed to 1% applied strain. Simulations were performed using both plane strain and bonded boundary conditions (see text), and with both power law and Voce hardening equations. Each value of plastic strain corresponds to a distinct simulation with a random distribution of crystallographic orientations per grain.

suggests that crystal plasticity produces higher plastic strains, on average, than J2-plasticity.

Summary

Finite element models with crystal plasticity constitutive relations and high-performance computing allow for further exploration into the statistics associated with random microstructure and material defects. In this section, the strain concentration at a notch was computed for many realizations of crystallographic texture. The resulting statistics show a wide variation in the strain concentration. The variation is further demonstrated when compared to a deterministic J2 calculation.

Table 2. Crystal Plasticity Constants [9] for Brass [10]

Material Constant	Units	Power Law Hardening	Voce Hardening
C_{11}	[GPa]	168.4	168.4
C_{12}	[GPa]	121.1	121.4
C_{44}	[GPa]	75.4	75.4
$\dot{\gamma}_o$	[time^{-1}]	1.0	1.0
$\dot{\gamma}_{min}$	[time^{-1}]	1x10^{-5}	1x10^{-5}
$\tau_{crss,o}$	[MPa]	280.0	280.0
m	-	33.0	33.0
A	[MPa]	525.7	193.5
n	-	0.5248	4000.4

Table 3. Moments of the Distribution of Maximum Local Plastic Strain

Hardening Law [9]	Boundary Condition	μ [%]	σ [%]	μ/σ [%]
Power	Plane Strain	26.76	3.36	12.56
Power	Bonded	31.70	3.48	10.98
Voce	Plane Strain	25.84	4.79	18.54
Voce	Bonded	31.89	5.75	18.03

Note: μ denotes the mean, and σ the standard deviation.

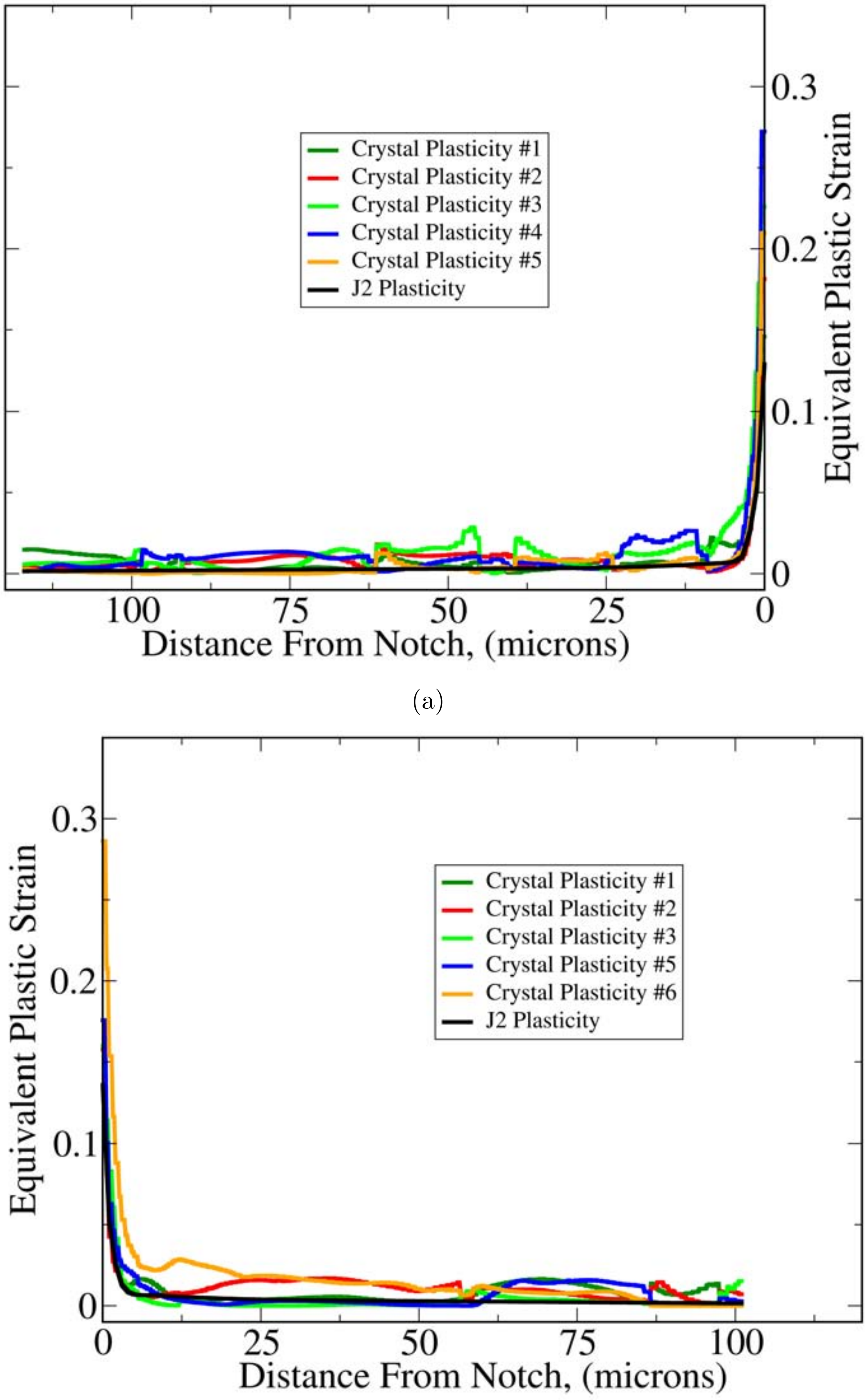

(a)

(b)

Figure 18. Equivalent plastic strain emanating from the (a) left and (b) right corner of the notch.

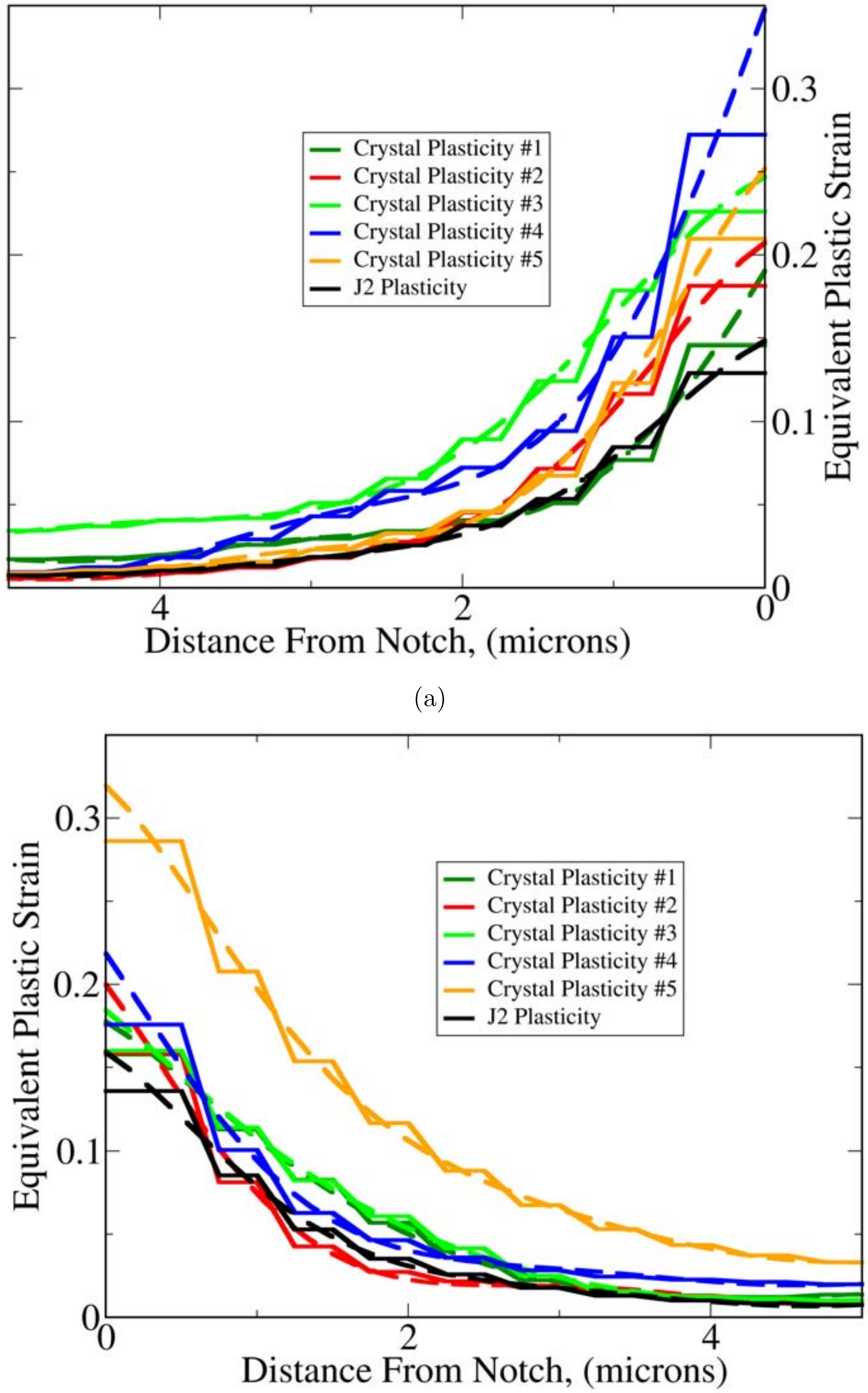

(a)

(b)

Figure 19. Local view of the equivalent plastic strain emanating from the (a) left and (b) right corner of the notch.

Discussion

Consider a thin plate with a hole at its center, made from a single crystal of brass. Because it is both elastically and plastically anisotropic, its mechanical response will depend on the relationship between the applied deformation and the crystallographic orientation of the material, as demonstrated in Figure 16. Thus, it is not surprising that when a hole is inserted into a polycrystalline microstructure, and its size is less than that of the surrounding grains, then its mechanical response is sensitive to the particular grain (and perhaps the immediate environment) in which it happens to reside. This might explain why the EBSD images for $R = 1$ and $R = 1/7$, in Figures 5 and 6, show behavior that is not consistent with classical continuum plasticity. (The same argument explains why the crystallographic reorientation, and thus presumably the plastic deformation, is strongly perturbed by the neighboring microstructure in cases where the hole is moderately larger than the grains, as in the case of $R = 7$ in Figures 5 and 6.) If another small hole were machined into a different microstructural environment, a quite different outcome might occur. However, more experiments and simulations are required to provide conclusive evidence in the present case. Nonetheless, the corresponding simulations shown in Figure 16 strongly support this idea.

The idea is further supported in Figure 19. This figure demonstrates two significant ideas about the local crystallography. First, ignoring the slight eccentricity, the peak strain concentration is entirely dependent on the local crystal orientation. Crystal realization #4 has a peak strain at the left corner of the notch, while realization #5 has a peak strain at the right corner of the notch. Second, the slight eccentricity directs our intuition to expect the peak concentration at a given corner; however, the local crystal orientation is shown to overpower slight geometric preferences. Intuition appears to be fragile. Further exploration into these competing effects is necessary. However, the take-away observation is as follows: the randomness of the microstructure affects the peak strain concentration *and* where it occurs.

Regardless of the rationale, these results suggest a more general theme that is of critical importance in cases where a governing or critical phenomenon (plasticity near a hole, in the present case) occurs on a length scale that is comparable to, or smaller than, the characteristic length scale of the internal structure of an inhomogeneous medium (the grain size, in the present case). This can occur in a wide range of scenarios, e.g. the mechanical response of a defected material, and the behavior of small structures. In such cases, the inherent variability of that very internal structure will translate into uncertainty about the properties that are dictated by the phenomenon in question. This concept is illustrated in Figure 20.

Sandia has invested vast resources in the development and implementation of high-fidelity, deterministic computer models; and in the deployment of high-performance computing re-

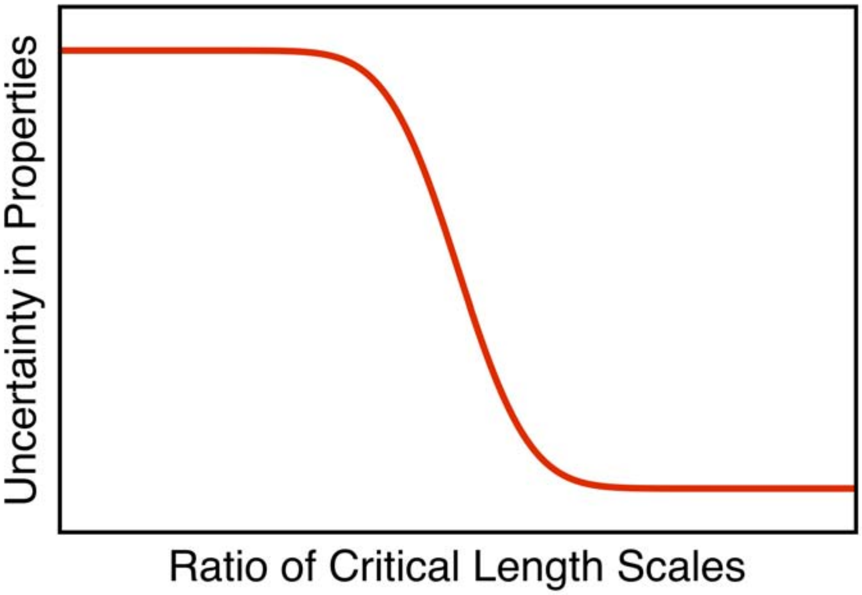

Figure 20. Schematic of the uncertainty in materials property as a function of the ratio in characteristic length scales between critical phenomenon and internal structure. In the present study, the critical phenomenon is the concentration of plastic strain at an engineered defect (i.e. a hole), and the relevant length scales are the size of the hole (and thus of the plastic zone), and that of the grains.

sources with which to exercise them. These efforts are obviously of critical importance, and have yielded enormous benefit both inside and outside Sandia. However, as demonstrated in this work, there are cases where the properties of interest are not scalar, but rather statistical, and can therefore not be accurately captured by a deterministic treatment. Instead, it is necessary to couple the high-fidelity, deterministic models to a statistical treatment of the underlying variability in the material(s) of interest, to produce an accurate description of the uncertainty in the resultant properties and performance.

Conclusions

Brass sheet was annealed under varying conditions to produce a range of grain sizes, and then machined into tensile specimens. Microstructure-scale holes were then drilled into each specimen using a femto-second laser. Experiments and simulations of the uniaxial tension of the specimens were performed to ascertain the role of microstructure on the deformation behavior near the hole.

Electron backscatter diffraction experiments showed that, when the hole was several times the size of the grains, the crystallographic misorientation in the plastic zone had approximately the expected shape and alignment (with respect to the tensile axis), but was strongly perturbed by the microstructure in the hole's vicinity. However, when the hole was comparable to the grain size, the crystallographic misorientation data suggested that the concentration of plastic strain near the hole was not pronounced, and had no discernible relationship to the tensile geometry. When the hole was smaller than the grain size, no appreciable concentration of plastic strain was observed near the hole. Forward scatter experiments in the latter case showed a strong preference for single- and double-slip in the material near the hole, and these conditions could mask the manifestation of plastic deformation in the crystallographic misorientation.

Digital image correlation was used to directly map the in-plane strain components on the surfaces of the deformed specimens. These experiments indicated that plastic zones are present around the hole, but the magnitudes of the associated strains are comparable to those in neighboring grains which are more favorably oriented for slip. These results present initial evidence that greater care will need to be taken in predicting the strain concentration effects of defects as they approach the characteristic size of the underlying microstructure.

Finite element simulations of single, square crystals containing cylindrical holes were performed. These simple calculations showed that the amount and diffusivity of plastic deformation was highly dependent on the crystal orientation.

Finite element simulations of uniaxial tension were performed on a computer-generated microstructure containing a rounded slot. In order to collect statistics describing the sensitivity of plastic deformation to the local microstructural environment, a single finite element model was simulated many times with different random crystallographic orientations assigned to each grain. From each simulation, the maximum plastic strain was extracted from the slot's tip and distributed to approximate a probability density. The standard deviation of the maximum plastic strain was found to be nearly 20% of the mean.

These results demonstrate that in regimes where characteristic length scale of a material's internal structure approaches that of the phenomena that are critical in determining the material's properties, the inherent variability manifesting in that internal structure produces uncertainty in the properties. This is especially relevant to localized phenomena, like deformation near defects; and to components that are small relatively to the internal structure of the constituent material(s). In order to completely quantify a component's performance and reliability, deterministic models of its materials' physics must be combined with stochastic treatments of the materials' microstructures to reflect the inherently statistical nature of the real materials' properties.

Future Work

This work has helped to nucleate two new projects in Sandia's Advanced Certification Program, which will begin in FY10 and will address the influence of microstructure variability on uncertainty in the properties of welds. The FY10 projects are titled "Materials and Processes FMEA and QMU for Advanced Certification," and "Process Aware Material Models."

In a broader context, we assert that in a wide range of engineering applications, the impact that the variability in a material's processing and structure can have on its properties and performance, simply *cannot be safely ignored.* We must foster a significant and viable effort to establish generalized knowledge, procedures, and protocols for the implementation of deterministic models in a statistical, *nano-* and *micro-structure-driven* context that connects unavoidable variability in materials processing, to the inhomogeneity of its structure, to the statistics that describe the resultant properties, and finally to uncertainty in performance. As demonstrated by the present work, this can certainly be true in a number of "classical" engineering problems like defect mechanics. It is also of prime importance as we attempt to further miniaturize the components and systems that we design, manufacture, and deploy. By exercising Sandia's immense resources in high-performance, high-fidelity, deterministic, physical models, in a context that captures the inherent variability in both present and future engineering materials, we can establish a predictive, science-based capability that accurately captures not only the materials properties themselves, but also the statistics that underly those properties. Only in this way can we hope to robustly address the sources uncertainty in the performance and reliability of the systems that are critical to Sandia's missions.

References

[1] J. A. Rayne, Physics Review **112**, 1125 (1958).

[2] W. D. Pilkey, *Petersons Stress Concentration Factors*, John Wiley and Sons, New York, second edition, 1997.

[3] A. Ancona et al., Optics Express **16**, 8958 (2008).

[4] C. Fohl, D. Breitling, and F. Dausinger, High speed laser drilling of metals using a high repetition rate, high average power ultrafast fiber cpa system, in *Precise Drilling of Steel with Ultrashort Pulsed Solid-State Lasers*, pages 271–279, Spie-Int Soc Optical Engineering, Moscow, 2002.

[5] L. N. Brewer, D. P. Field, and C. C. Merriman, Mapping and assessing plastic deformation using ebsd, in *Electron Backscatter Diffraction in Materials Science*, Springer Science and Media Business, New York, second edition, 2009.

[6] M. A. Sutton, S. R. McNeill, J. D. Helm, and Y. J. Chao, Topics in Applied Physics **77**, 323 (2000).

[7] B. L. Boyce, P. L. Reu, and C. V. Robino, Metallurgical and Materials Transactions A **37A**, 2481 (2006).

[8] E. A. Holm and C. C. Battaile, Journal of the Minerals, Metals, and Materials Society **53**, 20 (2001).

[9] T. E. Buchheit, G. W. Wellman, and C. C. Battaile, International Journal of Plasticity **21**, 221 (2005).

[10] Y. Wang, Y. Zhou, and Y. Xia, Materials Science and Engineering A **372**, 186 (2004).

DISTRIBUTION:

1	MS 0889	B.L. Boyce, 01813
1	MS 0887	D.B. Dimos, 01800
1	MS 0824	H.H. Hirano, 01510
1	MS 0885	J.E. Johannes, 01810
1	MS 9151	J.S. Lash, 08960
1	MS 0959	J.P. McDonald, 02452
1	MS 1411	R.A. Roach, 01814
1	MS 0899	Technical Library, 9536 (electronic)
1	MS 0123	D. Chavez, LDRD Office, 1011

Sandia National Laboratories